

Wavelength-Selective, Narrowband Graphene Transistor with a Plasmon-Enhanced Pyroelectric Gate

Le Wei, Jingjing Qian, Liang Dong, and Meng Lu*

Herein, a wavelength-selective pyroelectric sensor based on a graphene field-effect transistor (gFET) with a plasmon-enhanced pyroelectric gate (PG) is reported. The PG gFET (PG-gFET) uses a poly(vinylidene fluoride-co-trifluoroethylene) or PVDF-TrFE membrane doped with plasmonic nanoparticles as the gate. Gold nanorods (AuNRs) or silver nanoparticles (AgNPs) are incorporated into the PVDF-TrFE membrane to enhance the photothermal conversion efficiency of PVDF-TrFE in a specific narrowband wavelength range. The wavelength-selective photothermal effect can optically modulate the gate potential of the PG-gFET; this, in turn, leads to a change in current through the graphene film of the transistor. The PG-gFET with AuNRs exhibits a maximum responsivity of $0.79 \mu\text{A mW}^{-1}$ at the wavelength of 660 nm. Replacing AuNRs with AgNPs in the PVDF-TrFE membrane results in tuning the plasmonic response of the transistor to 488 nm with a maximum responsivity of $0.68 \mu\text{A mW}^{-1}$. When plasmonic nanoparticles are absent from the PVDF-TrFE membrane, the maximum response wavelength of the transistor is shifted to a midinfrared regime at 3125 nm, which is associated with the C=C absorption of PVDF-TrFE. The ability of the PG-gFET to selectively respond to different light wavelengths will benefit many fields, including pyroelectric sensors, spectroscopy, and imaging.


1. Introduction

Pyroelectric detectors are widely used in detecting infrared (IR) radiation, motion, gas, flame, and chemical composition and exhibit the advantages of low cost and room-temperature

L. Wei, J. Qian, L. Dong, M. Lu
Department of Electrical and Computer Engineering
Iowa State University
Ames, IA 50011, USA
E-mail: menglu@iastate.edu

L. Dong
Microelectronics Research Center
Iowa State University
Ames, IA 50011, USA

M. Lu
Department of Mechanical Engineering
Iowa State University
Ames, IA 50011, USA

 The ORCID identification number(s) for the author(s) of this article can be found under <https://doi.org/10.1002/adpr.202300009>.

© 2023 The Authors. Advanced Photonics Research published by Wiley-VCH GmbH. This is an open access article under the terms of the Creative Commons Attribution License, which permits use, distribution and reproduction in any medium, provided the original work is properly cited.

DOI: 10.1002/adpr.202300009

operation.^[1–6] Generally, these detectors operate on the pyroelectric effect of ferroelectric materials, such as zinc oxide, gallium nitride, and poly(vinylidene fluoride-trifluoroethylene) (PVDF-TrFE), to convert temporal temperature changes into electrical signals.^[7] When the pyroelectric detector is connected to the gate of a field-effect transistor (FET), the output signal from the detector can be amplified by the transistor. Essentially, a temperature variation can cause spontaneous electrical polarization of the pyroelectric material; consequently, electrical charges will be generated across the pyroelectric material to tune the current flow between the source and drain terminals of the transistor.^[8–14] As a relatively recent member of the transistor family, graphene FETs (gFETs) have drawn great attention.^[15–19] By changing the voltage applied at the gate of gFET, the charge density and current flow in the graphene of gFET will be modulated.^[20–23] Further, by modifying the gate of gFET

with appropriate sensing materials and structures, the gFET can act as a biochemical or physical sensor.^[24–29] The pyroelectric materials are promising candidates for the sensory gate in photothermal sensitive gFETs.

It should be pointed out that most pyroelectric detectors to date are broadband.^[30–35] To respond to IR radiation within a spectrally narrow band, these detectors generally require an external optical filter. Because spectral filters are relatively bulky, costly, and sensitive to optical misalignment,^[36,37] integrated on-chip narrowband light absorption is highly desired for realizing compact pyroelectric detectors. Due to the ability to tune optical resonance, plasmonic nanomaterials and nanostructures have been used to improve photothermal conversion efficiency in a target narrow band for applications such as photocatalysis, photothermal imaging, optical sensing, and thermal therapy.^[38–42] We hypothesize that by incorporating appropriate plasmonic nanoparticles into the pyroelectric material of pyroelectric detectors, it will be possible to realize on-chip narrowband light absorption for the pyroelectric detector with high compactness and wavelength selectivity.

This article presents a wavelength-selective pyroelectric detector with an on-chip narrowband light absorber. The detector is formed with a gFET containing a pyroelectric gate (PG) of PVDF-TrFE doped with plasmonic nanoparticles. PVDF-TrFE is adopted here because its pyroelectric and optical properties can be flexibly adjusted by doping various nanomaterials.^[43–46]

The PG allows optically modulating changes in the drain-to-source current of the transistor with IR radiation. Owing to the plasmonic nanoparticles, the PVDF-TrFE membrane enables the selective absorption of narrowband light around the resonance wavelength of the plasmonic nanoparticles. The absorbed light alters the temperature of the gate. Therefore, the PVDF-TrFE membrane will be polarized, and the current flow through the graphene film of the transistor will be modulated. It is also noteworthy that the PVDF-TrFE membrane also serves as a freestanding substrate of the device to minimize the thermal mass. The low thermal conductivity of PVDF-TrFE also helps reduce thermal loss from the gate area, thus increasing the temperature changes at the gate of the device.

2. Results and Discussion

2.1. Design and Fabrication of PG-gFET

The PG-gFET detector (Figure 1a) consists of a PVDF-TrFE 15 μm -thick membrane, a monolayer graphene, two gold (Au) contacts for defining the source and drain terminals of the transistor, and a supporting frame. To effectively convert incident light to heat via the plasmonic effect, Au nanorods (AuNRs; size: 40 nm \times 20 nm) or Ag nanoparticles (AgNPs; diameter: \approx 20 nm) were mixed into the PVDF-TrFE solution. The metal nanoparticles can support collective oscillation of electrons, which give rise to the localized surface plasmon resonance (LSPR) modes.^[40–42] The metal nanoparticles can be designed to have specific sizes and shapes that control their LSPR modes and

the wavelength of light that they interact with. When the excitation light can be coupled into one or more LSPR modes, the AuNRs or AgNPs can strongly absorb the light and convert the absorption into heat. Figure 1b briefly describes the key steps of fabricating the pyroelectric detector. The AuNR- or AgNP-doped PVDF-TrFE solution was first spin-coated onto the surface of monolayer graphene on a copper foil. After the PVDF-TrFE layer was solidified at room temperature in air, the graphene layer was transferred onto the PVDF-TrFE membrane by wet-etching the copper foil. Subsequently, the obtained PVDF-TrFE membrane with the graphene layer was placed and suspended over a supporting frame. The source and drain contacts were then formed on top of the graphene layer by e-beam evaporation of a 100 nm-thick Au layer with the help of a shadow mask. The details of the fabrication process are described in Experimental Section. To examine the composite membrane of the AuNR-embedded PVDF-TrFE and graphene, an ion milling method was used to cut the composite for the scanning electron microscopic (SEM) examination. The SEM image (Figure 1c) indicates the dispersion of AuNRs in the composite membrane.

2.2. Characterization of Plasmonic Nanoparticle-Doped PVDF-TrFE with a Transferred Graphene

Figure 2a compares the Raman scattering spectra of the original graphene on the copper foil with the transferred graphene on the PVDF-TrFE membrane. Both the samples present two principal graphene bands at 1589 cm^{-1} (G band) and

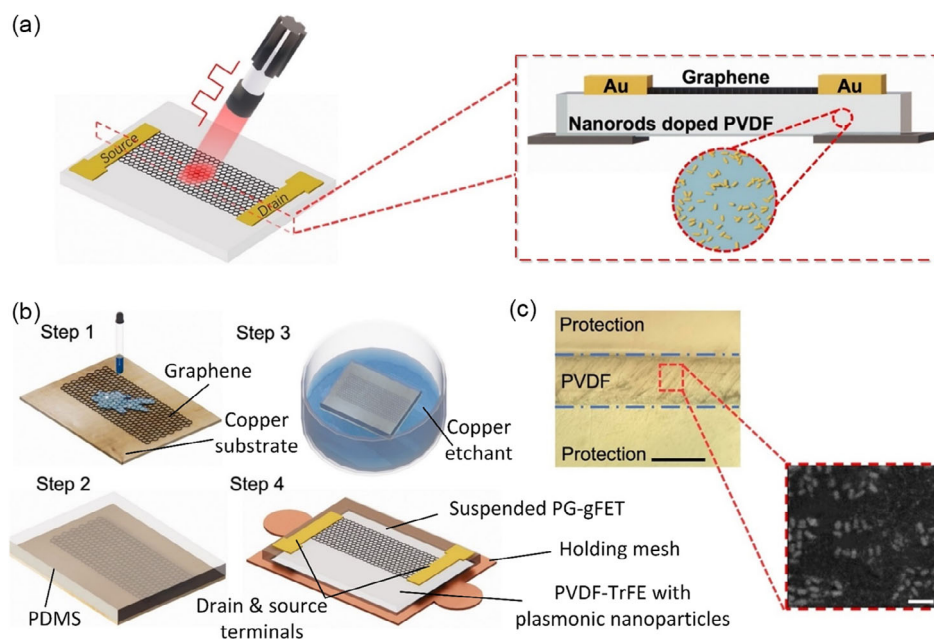


Figure 1. Pyroelectric gating gFET (PG-gFET) detector formed on a suspended PVDF-TrFE membrane doped with Au or Ag nanostructures. a) Schematic of the PG-gFET on an AuNR-doped PVDF-TrFE membrane. b) Major steps for fabricating the PG-gFET including (i) spin coating the solution of PVDF-TrFE containing Au nanorods on the surface of graphene with a copper substrate, (ii) baking the PVDF-TrFE membrane, (iii) removing the copper substrate via wet-etching, and (iv) transferring the PG-gFET membrane onto a mesh grid, followed by forming the contact pads for the drain and source terminals. c) Microscopic image for the cross section of the PG-gFET (scale bar: 20 μm). The inset shows the SEM image for the cross section of the PVDF-TrFE membrane embedded with AuNRs (scale bar: 200 nm).

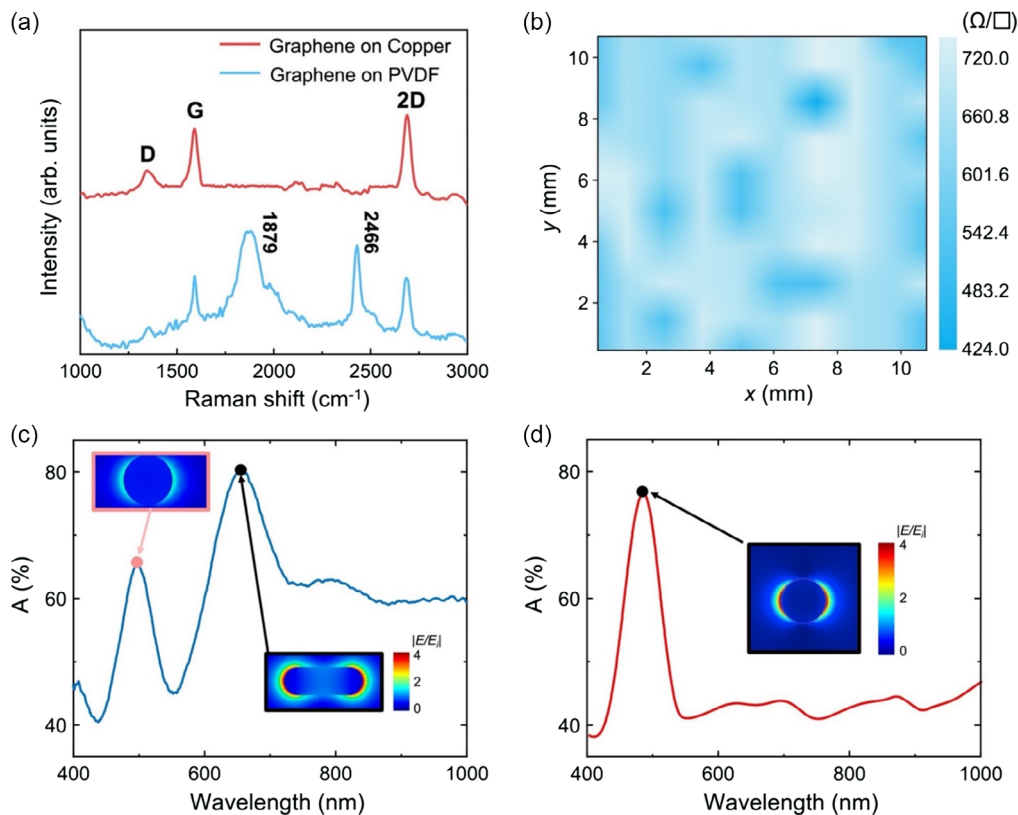


Figure 2. Characterization of the transferred graphene on top of AuNR-doped PVDF-TrFE membrane. a) Raman spectra of the monolayer graphene on the copper foil (red) and PVDF-TrFE membrane (blue). b) Sheet resistance distribution of the transferred graphene layer on the AuNR-doped PVDF-TrFE membrane. c) Absorption spectra of the AuNR-doped PVDF-TrFE membrane. The insets show the simulated near-field distributions for the longitudinal and axial LSPR modes at 500 and 660 nm, respectively, of the AuNRs. d) Absorption spectra of the PVDF-TrFE membrane doped with AgNPs. The inset shows the simulated near-field distribution for the LSPR mode of the AgNPs at 488 nm wavelength.

2644 cm^{-1} (2D band). The D band at 1325 cm^{-1} , which is associated with the defects within the carbon lattice, became less prominent for the PVDF-TrFE transferred graphene compared to that for the original graphene. To inspect the electrical property of the transferred graphene, a four-point probe method was used to measure the sheet resistance of graphene with a 1 mm increment along both x - and y -directions. The distribution map (Figure 2b) indicates a $590 \pm 103 \Omega \text{sq}^{-1}$ sheet resistance over the transferred graphene's $10 \times 10 \text{mm}^2$ area.

In addition to supporting the graphene layer, the PVDF-TrFE membrane also served as the narrowband light absorber and the PG of the transistor. The absorption signature wavelengths of the AuNR- and AgNP-doped PVDF-TrFE membranes were measured in the visible wavelength range. The absorption spectrum $A(\lambda)$ of the AuNR-doped PVDF-TrFE membrane exhibited two absorption peaks at $\lambda_{r1} = 500 \text{ nm}$ and $\lambda_{r2} = 660 \text{ nm}$. The resonance peak at 660 nm corresponds to the longitudinal LSPR mode (along the length of AuNRs), as shown in the simulated electric field distribution around $40 \text{ nm} \times 20 \text{ nm} \times 20 \text{ nm}$ AuNRs. Embedded in the PVDF-TrFE membrane, the longitudinal LSPR mode had a peak absorption efficiency above 80% and a full-width half-maximum (FWHM) of 60 nm. The other resonance at 500 nm wavelength is related to the axial LSPR resonance (see the inset in Figure 2c). Figure 2d shows the measured absorption spectrum

of the PVDF-TrFE membrane doped with 20 nm-diameter AgNPs; the resonance locates at $\lambda = 488 \text{ nm}$ with a 78% absorption efficiency and a 54 nm FWHM.

To estimate temperature distribution at the 15 μm -thick, AuNR-doped PVDF-TrFE membrane when exposed to incident light, we modeled the heat transfer process on the membrane using the finite element method (FEM) simulation (see details in Materials and Methods). Figure 3a shows the temperature distribution across the membrane when illuminated by a red laser beam (wavelength: 660 nm; power: 90 mW; beam size: 1 mm diameter). According to the electromagnetic simulation shown in Figure 2c, the light absorption coefficient of the membrane was set to 80%. At the ambient temperature of 20 $^{\circ}\text{C}$, the absorbed light can increase the central temperature of the membrane to 38 $^{\circ}\text{C}$. Figure 3b plots the dynamic temperature response at the center of the membrane when heated by the laser and cooled by shutting off the laser. The result shows that the central temperature could reach equilibrium within 70 ms.

2.3. Electrical and Optical Characterization of PG-gFET

Figure 4a shows the source-to-drain current I_{DS} of the PG-gFET under the drain-to-source voltage $V_{\text{DS}} = 4 \text{ V}$ and zero-gate bias voltage $V_{\text{G}} = 0 \text{ V}$ at room temperature. The transistors with

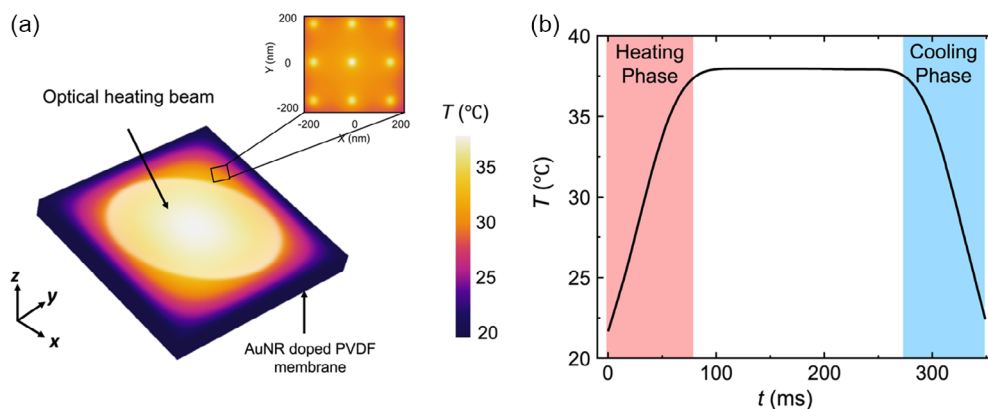


Figure 3. Thermodynamic simulation of light-induced temperature change. a) Temperature distribution of the suspended PVDF-TrFE membrane doped with AuNRs. The membrane was heated using a laser source ($P = 90$ mW, absorption coefficient = 80%) incident at the center of the membrane. The inset shows the close-up of the temperature distribution, where the bright spots indicate the dispersion of AuNRs. b) Dynamic temperature change as a function of time when the PVDF-TrFE membrane was heated and cooled.

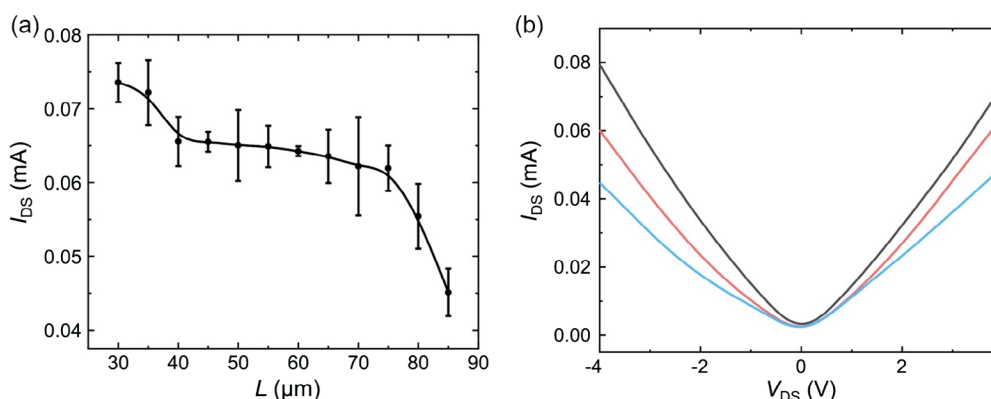


Figure 4. $I_{DS}-V_{DS}$ characterization of the PG-gFET. a) Measured I_{DS} as a function of channel length L between the source and drain terminals under $V_{DS} = 4$ V and $V_G = 0$. b) Representative $I_{DS}-V_{DS}$ curves of the PG-gFET with $L = 35, 55,$ and 80 μm under $V_G = 0$ with the unpolarized gate.

different channel lengths L were tested. When the value of L increased from 30 to 85 μm , the current I_{DS} dropped from 0.074 to 0.046 mA due to the increase in the channel resistance. Figure 4b compares the $I_{DS}-V_{DS}$ curves of the transistor with $L = 80, 55,$ and 35 μm with $V_G = 0$.

Next, optical responses of the PG-gFET were examined. Here, the pyroelectric membrane of the transistor was doped with AuNRs. The gate of the transistor was illuminated by an intensity-modulated laser (power $P = 90$ mW mm^{-2} ; wavelength $\lambda = 660$ nm; chopping frequency $f = 5$ Hz), and the change of source-to-drain current (ΔI_{DS}) was measured (Figure 5a). The laser-induced heating and subsequent natural cooling of the PVDF-TrFE membrane regulated the gate voltage of the transistor, thus changing the source-to-drain current. Figure 5b explains how I_{DS} varies at four consecutive phases of a heating-cooling cycle. When the laser beam is off, the PG potential is zero, and the Fermi level of graphene is at its Dirac point. Under a given V_{DS} , I_{DS1} is relatively low when the PVDF-TrFE PG is unpolarized under $V_G = 0$. When the laser excitation is turned on, the plasmonic nanoparticles can help to quickly heat the device. During the heating phase, the PVDF-TrFE membrane is polarized and produces a PG potential to shift the Fermi level, thus increasing the

current to I_{DS2} . When the temperature stabilizes, the PG potential disappears, and the current drops back to I_{DS1} . When the excitation light is turned off, the device starts to cool down, and the change in temperature causes the source-drain current to increase to I_{DS3} . When the device completely cools down to room temperature, the current decreases to I_{DS1} . Figure 5c plots the relative change in drain-to-source current $\Delta I_{DS}/I = |I_{DS} - I_0|/I_0$ as a function of time when $V_{DS} = 4$ V and the laser intensity was modulated using a 200 ms-period square wave signal. I_0 is the current output without laser input. The peak current was found to be $I_{DS2} = 0.076$ mA. The relative current change reached its maximum value within 60 ms. After the temperature stabilized at equilibrium, the output current dropped to zero within 120 ms. When the laser was turned off, the gate temperature decreased, thus reducing the current to $I_{\text{off}} = 0.052$ mA.

2.4. PG-gFET for IR and Visible Light Detection

2.4.1. Response of Undoped PG-gFET to Incident Light

Without any plasmonic nanoparticle doping in the PVDF-TrFE membrane, the C-H and C=C bonds of PVDF-TrFE can help to

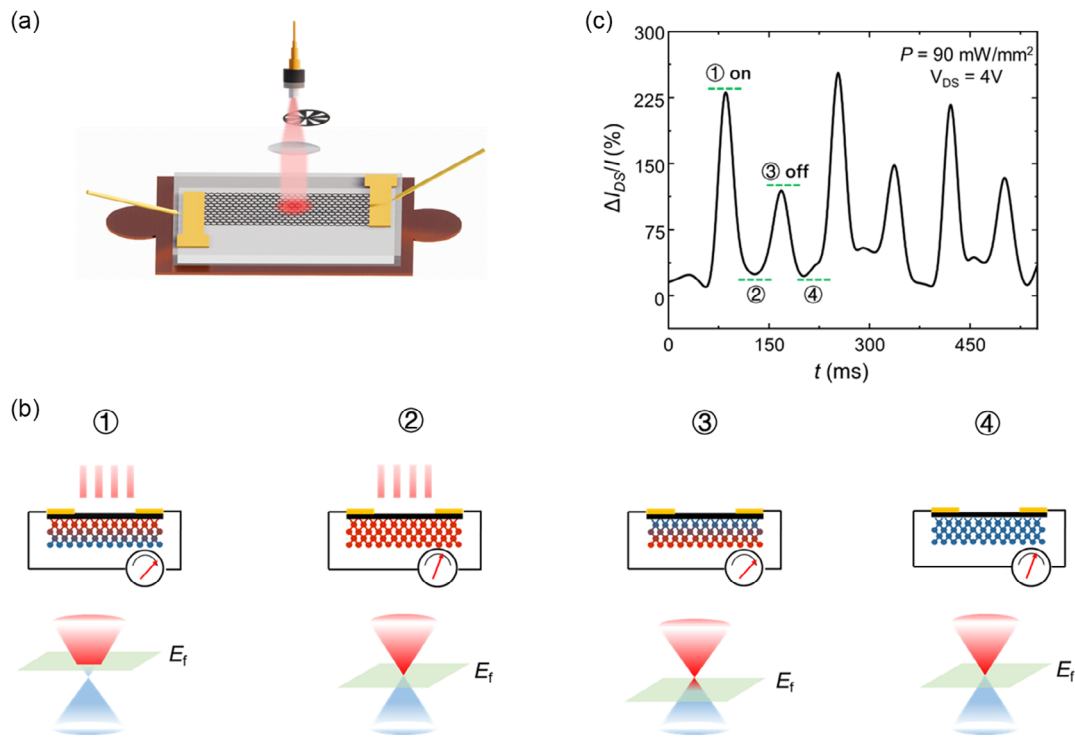


Figure 5. Operation of the PG-gFET detector. a) Schematic of the measurement setup to examine the dynamic response of the PG-gFET to an intensity-modulated incident light. b) The sensing mechanism of the PG-gFET. Each heating-cooling cycle includes four phases associated with the device temperature rise, stabilization, fall, and stabilization. The temperature change of the PVDF-TrFE membrane generates a pyroelectric potential, which can tune the graphene's Fermi level and thus increase the channel current. c) Relative change in drain-to-source current $\Delta I_{DS}/I = |I_{D-} - I_{D0}|/I_{D0}$ of the PG-gFET as a function of time when the intensity-modulated laser beam illuminated the transistor with $P = 90 \text{ mW mm}^{-2}$ and $V_{DS} = 4 \text{ V}$.

absorb light in the mid-IR wavelength range. **Figure 6a** shows the mid-IR absorption spectrum of the PVDF-TrFE membrane measured using a Fourier-transform infrared (FTIR) spectrometer. At 3125 and 2469 nm wavelengths, the absorption coefficients of the PVDF-TrFE membrane were 57% and 38%, respectively. The mid-IR absorption of PVDF-TrFE was utilized to control the source-to-drain current of the undoped PG-gFET. To test the

mid-IR response of the transistor, the emission from a silicon carbide (SiC) filament was filtered using a high-pass IR filter with a cutoff wavelength of 5500 nm and then was modulated by the chopper at a frequency of 5 Hz. At the device surface, the filtered IR emission was approximately 76 mW mm^{-2} . As a reference, a 660 nm-wavelength red light with the same power as the filtered IR emission was also used to examine the response of the

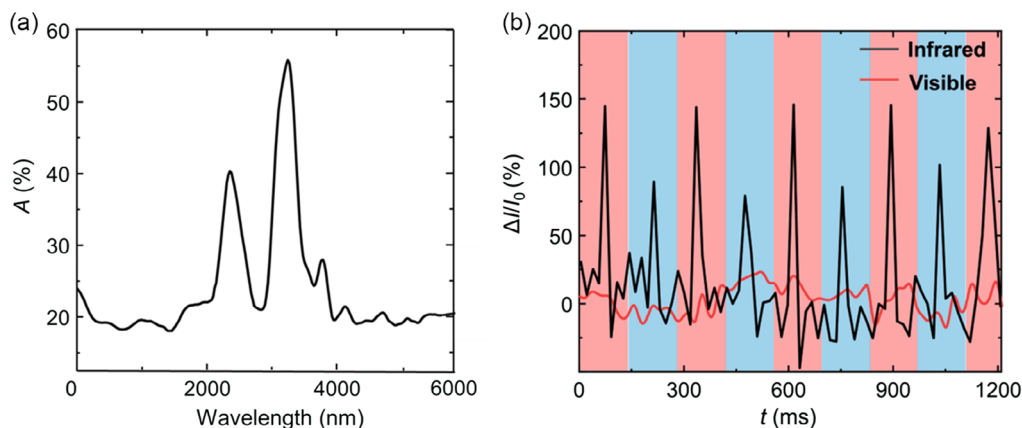


Figure 6. Mid-IR response of the undoped PG-gFET. a) Measured mid-IR absorption spectrum of the undoped PG-gFET, exhibiting two absorption peaks at 3125 and 2469 nm. b) Relative changes in drain-to-source current of the undoped PG-gFET when illuminated by IR light (black; 3100 nm wavelength) and visible light (red; 660 nm wavelength).

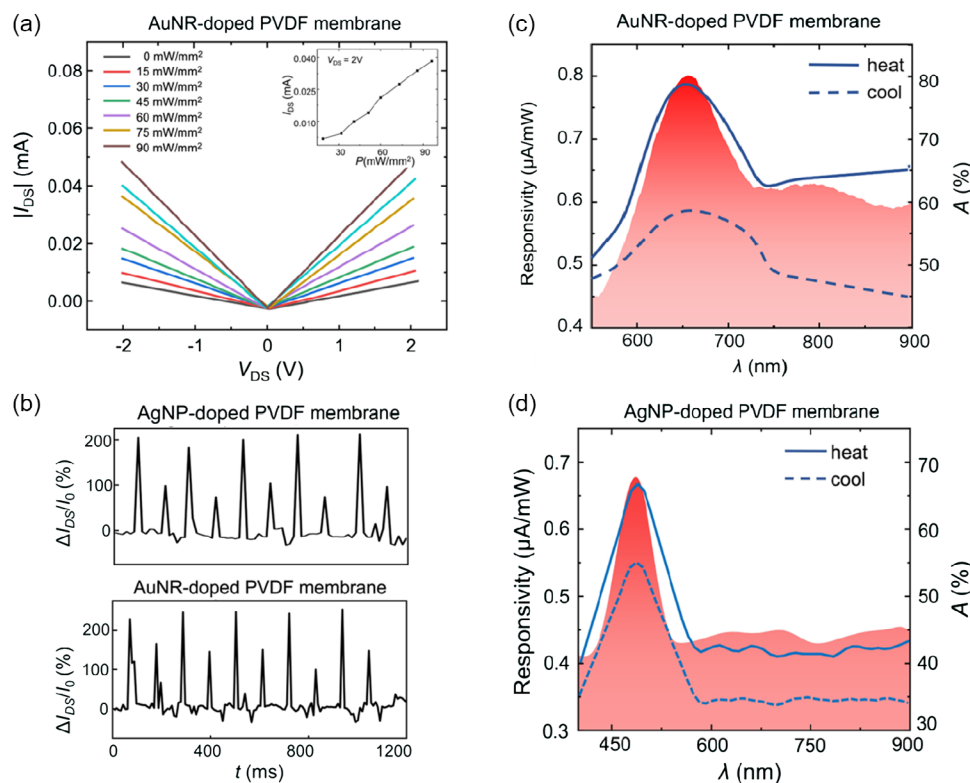


Figure 7. Characterization of PG-gFET doped with AuNRs and AgNPs. a) Measured $I_{DS}-V_{DS}$ curves of the PG-gFET under varying light excitation power from 1 to 90 mW mm^{-2} at $V_G = 0$. The inset shows I_{DS} as a function of light excitation power at $V_{DS} = 2 \text{ V}$. b) Relative change of I_{DS} over time when the AgNP- and AuNR-doped PG-gFETs were exposed to the intensity-modulated lasers at 488 and 660 nm, respectively. c) Spectral responsivity of AuNR-doped PG-gFET during the heating (solid line) and cooling (dashed line) phases, respectively. The absorbance of the AuNR-doped PVDF-TrFE membrane is shown in the background. d) Measured spectral responsivity of PG-gFET detector with AgNP for heating (solid line) and cooling (dashed line) phases. The absorbance of the AgNP-doped PVDF-TrFE membrane is shown in the background.

undoped PG-gFET. Figure 6b compares the relative changes of the output current from the mid-IR (black) and visible (red) excitations. The result shows that the undoped PG-gFET was almost insensitive to the visible light but exhibited a 150% increase in relative current change for the modulated IR light. As shown in the next section, by doping different plasmonic nanoparticles to the PVDF-TrFE layer, the PG-gFET could increase its response to visible light at different wavelengths.

2.4.2. Tuning Narrowband Responses of Plasmon-Enhanced PG-gFETs

Figure 7a shows $I_{DS}-V_{DS}$ curves of the AuNR-doped PG-gFET when exposed to the 660 nm-wavelength laser with different excitation power. The drain-to-source voltage was swept from $V_{DS} = -2$ to 2 V . As the laser power density increased from $P = 0$ to 90 mW mm^{-2} and V_{DS} was fixed at 2 V , I_{DS} was found to increase from 0.008 to 0.039 mA . The gate dependence of I_{DS} shows ambipolar behavior and is almost symmetric for both electron and hole doping; this result is directly related to the band structure of graphene, where both the electron and hole conduction are accessible by shifting the Fermi level. Figure 7b shows the responses of the PG-gFETs doped with AgNPs and AuNRs to the intensity modulation of the excitation light at 488 and

660 nm, respectively. As the LSPR is wavelength-dependent, the optical response of the PG-gFET varies with the excitation wavelength. Figure 7c shows the spectral response of the AuNR-doped PG-gFET in the wavelength range from 550 to 900 nm. The red background refers to the absorbance of the device. At the LSPR absorption peak wavelength of $\lambda_r = 660 \text{ nm}$, the PG-gFET exhibited a maximum responsivity of $0.79 \mu\text{A mW}^{-1}$, which was 1.8 times stronger than the off-resonance responsivity of $0.43 \mu\text{A mW}^{-1}$ at 900 nm wavelength. Figure 7d shows the spectral response of the transistor doped with AgNPs. At the LSPR absorption peak wavelength of $\lambda_r = 488 \text{ nm}$, the peak responsivity of the transistor increased to $0.68 \mu\text{A mW}^{-1}$, which was 1.5 times stronger than the off-resonance responsivity of $0.44 \mu\text{A mW}^{-1}$ at 900 nm wavelength. According to the result from Figure 7c,d, the spectral responses of the AuNR- and AgNP-doped PG-gFETs agreed well with the absorbance of the corresponding PVDF membranes used in the transistors.

3. Conclusions

This work demonstrated the wavelength-selective PG-gFET for both visible and IR sensing. The dispersions of AuNRs and

AgNPs inside the PVDF-TrFE membrane enhance narrowband light absorption of the PG-gFET near the LSPR absorption peak wavelengths of 660 and 488 nm, respectively. The plasmonic effect of these metal nanostructures improved the efficiency for converting the absorbed light to a temperature change at the gate of the transistor. The light-induced temperature change caused the PVDF-TrFE membrane to be polarized and thus changed the Fermi level of graphene; this, in turn, led to controlling the current flow in the graphene channel of the transistor. It has been shown that the drain-to-source current of the PG-gFET is sensitive to the coupling of the excitation light with the LSPR mode of the plasmonic nanoparticles. Therefore, the PG-gFET can be implemented as a narrowband pyroelectric detector. In addition, the PVDF-TrFE membrane itself showed considerable IR absorbance at 2469 and 3125 nm. These signature absorptions may allow the PG-gFET to operate as a sensor in the mid-IR light regime.

The future work will focus on improving the device performance from the following three aspects. First, pyroelectric materials, such as AlN and LiNbO₃, that have a higher pyroelectric coefficient may be used to replace PVDF-TrFE as the gate material of PG-gFET. The plasmonic nanostructures could be directly formed on one side of the pyroelectric membrane to absorb light, while the graphene layer could be transferred onto the other side, thus forming a new PG-gFET. Second, it is possible to incorporate plasmonic particles of different sizes at designated regions of a single pyroelectric membrane; this will allow forming of different PG-gFETs, with each transistor being able to respond to a specified narrow band. In addition, transition metal dichalcogenide 2D materials, such as WS₂ and MoS₂ with an inherent bandgap, may be used to form PG-gFETs with a higher switching current ratio. A high on/off ratio is highly desired for improving the sensitivity of the PG-gFET to incident light.

4. Experimental Section

Preparation of AuNR- and AgNP-Doped PVDF-TrFE: Raw PVDF-TrFE powder (Solvane 250/P400) was purchased from Sigma-Aldrich. To prepare a solution, 20 mg of PVDF-TrFE powder was dissolved in a 50 mL dimethylformamide (DMF) to a weight-to-volume ratio of 15% for 8 h at 75 °C. Both AuNRs (GRCN660) and AgNPs (AGCB20) were obtained from NanoComposix. The coefficients of variation of both AuNRs and AgNPs' sizes are smaller than 10%, which warrants the reliable and repeatable LSPR absorption characteristics. The AuNRs or AgNPs in a sodium citrate solution were resuspended in the mixture of DMF and acetone; the DMF, acetone, and nanoparticle solution were mixed in a ratio of 1:1:0.1. The resuspended plasmonic nanoparticles were mixed into the PVDF-TrFE solution with a volume-to-volume ratio of 1:10 using an ultrasonic homogenizer for 2 h at 60 °C.

Transfer of Graphene Using PVDF-TrFE: The PVDF-TrFE solution was spin-coated onto a monolayer graphene-coated copper foil at a speed of 2000 rpm for 45 s. After the spin coating, the sample was baked at 160 °C for 4 h to completely evaporate solvents and dry the PVDF-TrFE membrane. The thickness of the PVDF-TrFE membrane was measured using a stylus profiler (XP-1, AMBIOS Technology). To transfer the graphene, the PVDF-TrFE-coated sample was placed in a copper etchant (667528, Sigma-Aldrich) for 15 min to remove the copper foil. A supporting wire-mesh frame was then used to scoop the sample from the etchant. The sample was then rinsed with deionized water and baked in an oven at 100 °C overnight to clean the graphene. Finally, 100 nm-thick gold electrodes were formed at the device using an electron beam evaporator (BJD-1800, Temescal) through a shadow mask.

Characterization of Transferred Graphene Membrane: Raman spectra were taken using the BWTEK Voyage confocal Ramam system with $\lambda = 532$ nm laser source. The sheet resistance of the transferred graphene was measured using a four-point probe (SP4-62045TBS, Signatone) over the entire device area of 10×10 mm² with an incremental of 1 mm in both *x*- and *y*-directions. The absorption characteristics of the AuNR- and AgNP-doped samples were measured using a home-built transmission measurement setup and an FTIR spectrometer (FTS 7000, DigiLab) for visible and mid-IR ranges, respectively.

Transfer Characteristics under Visible and IR Excitations: The measurement was performed using 660 and 488 nm-wavelength laser sources for visible light. The laser output was collimated and polarized before being projected onto the device under test. The PG-gFET outputs were measured using a semiconductor parameter analyzer (4155B, HP) when the intensity of the laser was modulated at 5 Hz using an optical chopper. The 660 nm laser source's emission power was adjusted between 0 and 90 mW. The light source was switched to a SiC filament source for IR pyroelectric sensing. The SiC filament emission passed through a long-pass IR filter, an IR collimation lens, and the optical chopper. At the device surface, the filtered IR emission was measured to be 76 mW mm⁻².

Numerical Modeling: 3D finite-difference time-domain (FDTD) simulations were performed to simulate the LSPR phenomena of gold and silver nanoparticles embedded in the PVDF films. A commercial software package (FDTD solution, Lumerical Inc.) was used to facilitate the simulation. The simulation region was set to a single nanoparticle and truncated using the perfectly matched layer (PML) boundary conditions along all six sides to properly absorb incident radiation. The nanoparticle was illuminated with a normally incident, unit magnitude plane wave with an electric field polarization along tuned to excite the LSPR modes. Monitors were placed in close proximity to PMLs to calculate the amount of reflected and transmitted power as a function of wavelength. A uniform fine mesh size of 1 nm was used within the simulation domain. The optical properties of gold and silver were respectively taken from Johnson and Christy and Palik's handbook, and then fit by the multicoefficient model in the wavelength range from 400 to 900 nm. The refractive index and extinction coefficient of PVDF film was set at $n_{\text{PVDF}} = 1.5$ and $k_{\text{PVDF}} = 0$ without wavelength dispersion. The near-field distributions (Figure 2c,d) near the metal nanoparticles were calculated at the resonant wavelength and plotted using MATLAB.

Thermodynamic Modeling: The temperature distribution across the pyroelectric membrane was modeled using FEM (COMSOL Multiphysics 5.5). The simulation domain was discretized using 4-noded tetrahedral meshes. The boundary condition of a constant room temperature of 20 °C was applied at the lateral boundaries around the membrane. The top and bottom sides of the membrane were terminated using the open boundary to imply their contact with the surrounding air at room temperature. The absorption of 90 mW laser radiation induced a constant heat source of 72 mW mm⁻² at the center area (diameter: 1 mm) with an absorption coefficient of 80%. In the pyroelectric membrane, we added a 100 × 100 array of AuNRs as absorbers and assumed that all the AuNRs absorb the light uniformly. To convert the photon energy into heating energy, a time-dependent solver was used to solve Poisson's equation for heat transfer, $\frac{\partial^2 T}{\partial x^2} + \frac{\partial^2 T}{\partial y^2} + \frac{\partial^2 T}{\partial z^2} - \frac{\rho C_p}{k} \frac{\partial T}{\partial t} + \frac{\dot{e}_{\text{gen}}}{k} = 0$, where *T* represents the temperature value at each mesh node, \dot{e}_{gen} is the heat generation rate (W m⁻³) at the heat source, *k* denotes the heat conductivity, ρ is the material density, and *C_p* is the specific heat capacity. Interfaces between the materials were treated using the equivalent conductivity, $K_s = \frac{2k_1 k_2}{k_1 + k_2}$, where *k₁* and *k₂* denote the heat conductivities of the materials in contact, respectively. The heat conductivity, heat capacity at constant pressure, and density of the materials, including air and PVDF, were taken from the COMSOL's built-in material library.

Acknowledgements

This work was supported by the United States National Science Foundation under Award Nos. ECCS 17-11839 and ECCS 16-53673.

Any opinions, findings, and conclusions, or recommendations expressed in this material are those of the author(s) and do not necessarily reflect the views of National Science Foundation. The authors declare no competing financial interests.

Open access funding provided by the Iowa State University Library.

Conflict of Interest

The authors declare no conflict of interest.

Data Availability Statement

The data that support the findings of this study are available from the corresponding author upon reasonable request.

Keywords

graphene transistor, infrared detector, plasmonics, pyroelectric effect

Received: January 10, 2023

Revised: March 8, 2023

Published online:

- [1] Y. Yang, H. Zhang, G. Zhu, S. Lee, Z.-H. Lin, Z. L. Wang, *Acs Nano* **2013**, *7*, 785.
- [2] J. Yun, M.-H. Song, *IEEE Sens. J.* **2014**, *14*, 1482.
- [3] Y. Wang, J. Song, L. Dong, M. Lu, *J. Opt. Soc. Am. B* **2016**, *33*, 2472.
- [4] M. Kumar, D.-K. Ban, J. Kim, *Mater. Lett.* **2018**, *225*, 46.
- [5] T. D. Dao, S. Ishii, A. T. Doan, Y. Wada, A. Ohi, T. Nabatame, T. Nagao, *Adv. Sci.* **2019**, *6*, 1900579.
- [6] L. Dong, R. Yue, L. Liu, X. Wang, J. Liu, T. Ren, *Int. J. Infrared Millim.* **2003**, *24*, 1341.
- [7] A. Pecora, L. Maiolo, F. Maita, A. Minotti, *Sens. Actuators A-Phys* **2012**, *185*, 39.
- [8] N. T. Tien, Y. G. Seol, L. H. A. Dao, H. Y. Noh, N. E. Lee, *Adv. Mater.* **2009**, *21*, 910.
- [9] Stadlober, Zirkel, Leising, Gaar, Graz, Bauer-Gogonea, Bauer, *IEEE Trans. Dielectr. Electr. Insul.* **2006**, *13*, 1087.
- [10] J. Chang, C. H. Shin, Y. J. Park, S. J. Kang, H. J. Jeong, K. J. Kim, C. J. Hawker, T. P. Russell, D. Y. Ryu, C. Park, *Org. Electron.* **2009**, *10*, 849.
- [11] U. Sassi, R. Parret, S. Nanot, M. Bruna, S. Borini, D. De Fazio, Z. Zhao, E. Lidorikis, F. H. Koppens, A. C. Ferrari, A. Colli, *Nat. Commun.* **2017**, *8*, 14311.
- [12] R. Zheng, M. Y. Yan, C. Li, S. Q. Yin, W. D. Chen, G. Y. Gao, J. M. Yan, Y. Chai, *Nanoscale* **2021**, *13*, 20657.
- [13] M. Zirkel, A. Haase, A. Fian, H. Schön, C. Sommer, G. Jakopic, G. Leising, B. Stadlober, I. Graz, N. Gaar, R. Schwödiauer, S. Bauer-Gogonea, S. Bauer, *Adv. Mater.* **2007**, *19*, 2241.
- [14] H. Fang, Z. Lin, X. Wang, C.-Y. Tang, Y. Chen, F. Zhang, Y. Chai, Q. Li, Q. Yan, H. L. W. Chan, J.-Y. Dai, *Opt. Express* **2015**, *23*, 31908.
- [15] K. S. Novoselov, A. K. Geim, S. V. Morozov, D. Jiang, Y. Zhang, S. V. Dubonos, I. V. Grigorieva, A. A. Firsov, *Science* **2004**, *306*, 666.
- [16] F. Chen, J. Xia, D. K. Ferry, N. Tao, *Nano Lett.* **2009**, *9*, 2571.
- [17] M. Freitag, M. Steiner, Y. Martin, V. Perebeinos, Z. Chen, J. C. Tsang, P. Avouris, *Nano Lett.* **2009**, *9*, 1883.
- [18] I. Meric, M. Y. Han, A. F. Young, B. Ozyilmaz, P. Kim, K. L. Shepard, *Nat. Nanotechnol.* **2008**, *3*, 654.
- [19] M. Dudek, R. Kowderziej, A. Pianelli, J. Parka, *Sci. Rep.* **2021**, *11*, 74.
- [20] A. Das, S. Pisana, B. Chakraborty, S. Piscanec, S. K. Saha, U. V. Waghmare, K. S. Novoselov, H. R. Krishnamurthy, A. K. Geim, A. C. Ferrari, A. K. Sood, *Nat. Nanotechnol.* **2008**, *3*, 210.
- [21] F. Xia, T. Mueller, R. Golizadeh-Mojarad, M. Freitag, Y.-M. Lin, J. Tsang, V. Perebeinos, P. Avouris, *Nano Lett.* **2009**, *9*, 1039.
- [22] F. Schwierz, *Nat. Nanotechnol.* **2010**, *5*, 487.
- [23] L. Britnell, R. V. Gorbachev, R. Jalil, B. D. Belle, F. Schedin, A. Mishchenko, T. Georgiou, M. I. Katsnelson, L. Eaves, S. V. Morozov, N. M. R. Peres, J. Leist, A. K. Geim, K. S. Novoselov, L. A. Ponomarenko, *Science* **2012**, *335*, 947.
- [24] Y. Ohno, K. Maehashi, Y. Yamashiro, K. Matsumoto, *Nano Lett.* **2009**, *9*, 3318.
- [25] B. J. Kim, H. Jang, S.-K. Lee, B. H. Hong, J.-H. Ahn, J. H. Cho, *Nano Lett.* **2010**, *10*, 3464.
- [26] Y. Ohno, K. Maehashi, K. Matsumoto, *J. Am. Chem. Soc.* **2010**, *132*, 18012.
- [27] F. Xia, D. B. Farmer, Y. M. Lin, P. Avouris, *Nano Lett.* **2010**, *10*, 715.
- [28] L. Vicarelli, M. S. Vitiello, D. Coquillat, A. Lombardo, A. C. Ferrari, W. Knap, M. Polini, V. Pellegrini, A. Tredicucci, *Nat. Mater.* **2012**, *11*, 865.
- [29] P. Snapp, P. Kang, J. Leem, S. Nam, *Adv. Funct. Mater.* **2019**, *29*, 1902216.
- [30] M. Aleks, C. Jagtap, V. Kadam, G. Kolev, K. Denishev, H. Pathan, *Eng. Sci.* **2021**, *16*, 82.
- [31] M. Shankar, J. B. Burchett, Q. Hao, B. D. Guenther, D. J. Brady, *Opt. Eng.* **2006**, *45*, 106401.
- [32] S. G. Porter, *Ferroelectrics* **1981**, *33*, 193.
- [33] W. Jie, J. Hao, *Nanoscale* **2014**, *6*, 6346.
- [34] C. Baeumer, D. Saldana-Greco, J. M. P. Martinez, A. M. Rappe, M. Shim, L. W. Martin, *Nat. Commun.* **2015**, *6*, 6136.
- [35] E. S. Kulkarni, S. P. Heussler, A. V. Stier, I. Martin-Fernandez, H. Andersen, C.-T. Toh, B. Özyilmaz, *Adv. Opt. Mater.* **2014**, *3*, 34.
- [36] J. W. Stewart, J. H. Vella, W. Li, S. Fan, M. H. Mikkelsen, *Nat. Mater.* **2020**, *19*, 158.
- [37] L. Dong, R. Yue, L. Liu, S. Xia, *Sens. Actuators A: Phys.* **2004**, *116*, 257.
- [38] P. K. Jain, X. Huang, I. H. El-Sayed, M. A. El-Sayed, *Acc. Chem. Res.* **2008**, *41*, 1578.
- [39] Q. Wang, L. Liu, Y. Wang, P. Liu, H. Jiang, Z. Xu, Z. Ma, S. Oren, E. K. Chow, M. Lu, L. Dong, *Sci. Rep.* **2015**, *5*, 18567.
- [40] S. Hwang, J. Nam, S. Jung, J. Song, H. Doh, S. Kim, *Nanomedicine* **2014**, *9*, 2003.
- [41] Y. Zhao, Y. Huang, X. Zhao, J. F. McClelland, M. Lu, *Nanoscale* **2016**, *8*, 19204.
- [42] Y. Zhao, L. Liu, X. Zhao, M. Lu, *Appl. Phys. Lett.* **2016**, *109*, 071108.
- [43] R. Kumaran, S. D. Kumar, N. Balasubramanian, M. Alagar, V. Subramanian, K. Dinakaran, *J. Phys. Chem. C* **2016**, *120*, 13771.
- [44] L. Xing, Y. Nie, X. Xue, Y. Zhang, *Nano Energy* **2014**, *10*, 44.
- [45] S. Cha, S. M. Kim, H. Kim, J. Ku, J. I. Sohn, Y. J. Park, B. G. Song, M. H. Jung, E. K. Lee, B. L. Choi, J. J. Park, Z. L. Wang, J. M. Kim, K. Kim, *Nano Lett* **2011**, *11*, 5142.
- [46] L. Wei, H. Monshat, J. Qian, L. Dong, M. Lu, *Adv. Opt. Mater.* **2021**, *9*, 2101147.